PAPER

Check for updates

Multifunctional NaYF$_4$:Nd/NaDyF$_4$ nanocrystals as a multimodal platform for NIR-II fluorescence and magnetic resonance imaging†

Junwei Zhao, [iD] ‡[bc] Huishan Hu,‡[c] Wenquan Liu[a] and Xin Wang*[a]

Recently, multimodal imaging nanoprobes based on the complementary advantages of various imaging methods have attracted considerable attention due to their potential application in the biomedical field. As important bioimaging nanoprobes, lanthanide-doped nanocrystals (NCs) would be expected to improve the related biophotonic technology through integrated multimodal bioimaging. Herein, water-soluble and biocompatible NaYF$_4$:Nd/NaDyF$_4$ NCs were prepared by a solvothermal method combined with hydrophobic interaction with phospholipids as a capping agent. The NaYF$_4$:Nd/NaDyF$_4$ NCs exhibit excellent colloidal stability under physiological conditions. Compared with the bare NaYF$_4$:Nd^{3+} NCs, the second near-infrared (NIR-II, 1000–1700 nm) fluorescence intensities of Nd^{3+} ions in the NaYF$_4$:Nd/NaDyF$_4$ core−shell NCs at the emissions of 1058 nm and 1332 nm are enhanced by 3.46- and 1.75-fold, respectively. Moreover, the r_2 value of NaYF$_4$:Nd/NaDyF$_4$ NCs as T_2-weighted contrast agents is calculated to be 44.0 mM^{-1} s^{-1}. As a novel multimodal imaging nanoprobe, the NaYF$_4$:Nd/NaDyF$_4$ NCs can be employed for both NIR-II fluorescence and magnetic resonance imaging (MRI). The phospholipid-modified NaYF$_4$:Nd/NaDyF$_4$ NCs demonstrate *in vitro* and *in vivo* multimodal NIR-II fluorescence imaging and MRI of HeLa cells and tumors, respectively. This study provides an effective strategy for the development of novel multimodal probes for the medical application of nanomaterials.

Introduction

As a new biomedical imaging approach, nanotechnology has been widely applied in the early detection and diagnosis of diseases. In the past few decades, traditional medical imaging technologies, such as magnetic resonance imaging (MRI), computed tomography, positron emission tomography, and photoacoustics have played important roles in the diagnosis and treatment of diseases.[1–4] Owing to the inevitable limitations of each monomodal imaging technology, however, it is difficult to meet the requirements of spatial resolution and sensitivity for modern medical imaging.[5] Fortunately, the multimodal imaging approach combined with the respective merits of mono-modal imaging can provide multiple complementary imaging information in the diagnosis of diseases.[6–8] So far, many strategies for constructing hybrid nanoparticles (NPs) have been developed by encapsulating or conjugating fluorescent dyes, magnetic nanocrystals (NCs), upconversion NPs, rare earth complexes and radioactive reagents.[4,9–11] In our previous work, several nanocomposites or NCs have been developed for multimodal bioimaging nanoprobes, such as poly(DL-lactic-*co*-glycolic acid) coated NaYF$_4$:Yb, Er@NaGdF$_4$/doxorubicin nanocapsules, Fe$_3$O$_4$ nanoclusters, polyacrylic acid-NaMnF$_3$@-doxorubicin hybrid nanocomposites, ultrasmall Mn^{2+}-doped NaNdF$_4$ NCs, ZnPc/NaGdF$_4$:Yb,Er nanoclusters and folic acid-chitosan-coated NaYF$_4$:Yb/Er nanocrystals.[12–17] However, to construct desired multimodal imaging nanoprobes with high sensitivity, high spatial resolution and deep tissue penetration is still a major challenge.

Recently, fluorescence imaging has attracted more and more attention in life science and medical fields due to its fast feedback, high sensitivity and high spatial–temporal resolution.[15,18–21] In particular, fluorescence imaging in the second near infrared (NIR-II, 1000–1700 nm) window has been widely used in basic scientific research and clinical application due to its advantages of high sensitivity and high spatiotemporal resolution with the increase of tissue penetration depths. Compared with fluorescence imaging in the visible and the first near-infrared (NIR-I, 700–950 nm) regions, NIR-II fluorescence imaging significantly reduces the scattering loss, which makes it possible to observe the deep organisms of living animals with a higher spatial resolution.[22] Because the NIR-II window is

[a]Henan Key Laboratory of Photovoltaic Materials, Henan University, Kaifeng 475004, P. R. China. E-mail: xwang2008@vip.henu.edu.cn

[b]Materials Science and Engineering School, Henan Key Laboratory of Special Protective Materials, Luoyang Institute of Science and Technology, Luoyang 471023, P. R. China

[c]CAS Key Laboratory of Nano-Bio Interface, Suzhou Institute of Nano-Tech and Nano-Bionics, Chinese Academy of Sciences, Suzhou 215125, P. R. China

† Electronic supplementary information (ESI) available. See DOI: 10.1039/d0na00846j

‡ These authors contributed equally.

considered to be one of the optimal regions for optical bio-imaging, it is an urgent task to develop fluorescence probes with NIR-II emission capability. Although the existing NIR-II fluorophores are relatively lacking, there currently exist four candidates: quantum dots,[23–27] single-walled carbon nanotubes,[28–30] organic dye molecules,[31,32] and conjugated polymers.[3] However, there are some major limitations to the above mentioned fluorophores.[19] In contrast, lanthanide (Ln)-based NCs (*e.g.* Er^{3+}, Tm^{3+}, Ho^{3+}, Pr^{3+} and Nd^{3+}) as a new generation of NIR-II nanoprobes have many advantages, such as no photobleaching, long photoluminescence lifetimes, low long-term cytotoxicity and narrow emission band widths, which have gained more attention recently for bioimaging applications.[19,33] Among the candidates, Nd^{3+}-doped NCs arise as pioneers for NIR-II imaging due to their easy fabrication procedures and non-heating excitation bands in the biological transparency window.[19] The Nd^{3+} ions in NCs with different host matrices are able to emit NIR-II fluorescence under the excitation of near-infrared light. Therefore, the Nd^{3+} doped NCs have received extensive attention in the past few years.[34–39] Previous studies have shown that Nd^{3+} ions were mainly used as dopants, and the optimal doping molar ratio was controlled between 1% and 5%, as excessive concentrations of Nd^{3+} ions could cause a quenching effect and reduce the photoluminescence efficiency.[33,35,36,40] In addition, surface quenching due to defects or interactions with solvent molecules also affects their optical efficiency. Therefore, to obtain bright fluorescence signals, passivation shells would be employed for fabricating core–shell nanostructures, which shows a beneficial effect and has been proved in many studies.[35,36,39,41]

As one of the main means of physics and chemistry, MRI is widely used in the field of clinical imaging diagnosis, which relies on longitudinal (T_1) and transverse (T_2) relaxation times of endogenous water protons of the tissues to produce endogenous contrast. In previous studies, MRI, as a biological imaging method, provides more relative position details than other imaging methods, and can complement the biological information provided by other imaging methods.[42–46] Some rare earth elements (*i.e.*, Gd^{3+} and Dy^{3+}) as MRI contrast agents can be co-doped into upconversion NCs to achieve high tissue penetration depth utilizing multi-modal bioimaging.[12,47,48] Among them, Dy^{3+} ions have the advantages of a short electron relaxation time (~0.5 ps) and large magnetic moment (10.6 μ_B) and are considered to be an ideal contrast agent for T_2-weighted MRI.[49] Dy^{3+} doped upconversion NCs have been used as efficient T_2-weighted contrast agents in ultrahigh field MRI to obtain contrast enhancement.[48,50–52] Therefore, Dy^{3+} doped NCs are the ideal candidates for cancer imaging, which can lead to more accurate diagnosis. In order to be applied in biological environments, surface modification of NCs is necessary to enhance their water-solubility and biocompatibility.[53]

Significant research efforts have been made in the fabrication of Ln^{3+}-doped multifunctional nanocomposites to bridge the strengths of resolution and depth between MRI and NIR-II optical imaging. Herein, we prepared phospholipid-modified $NaYF_4$:Nd/$NaDyF_4$ (Lipo-$NaYF_4$:Nd/$NaDyF_4$) NCs as multimodal bioimaging nanoprobes for *in vitro* and *in vivo*

bioimaging of HeLa cells and tumors, respectively. Phospholipids possess a hydrophilic structure with low toxicity, and have been successfully used to modify various inorganic nanomaterials, such as quantum dots, iron, silica, and upconversion NCs.[54,55] The luminescent core of $NaYF_4$:Nd exhibited strong downconversion NIR-II luminescence under the excitation of 785 nm. With the growth of the protection $NaDyF_4$ layer on the $NaYF_4$:Nd core, the luminescence intensity at the emissions of 1058 and 1332 nm can be further enhanced by 3.46- and 1.75-fold, respectively, higher than that of bare $NaYF_4$:Nd NCs. Moreover, a high r_2 value of 44.0 mM^{-1} s^{-1} was calculated for the $NaYF_4$:Nd/$NaDyF_4$ NCs as T_2-weighted contrast agents. Therefore, accurate imaging can be obtained by intensified NIR-II luminescence imaging associated with a shell coating and T_2-weighted MRI imaging introduced by the Dy element. In addition, phospholipids have been employed as a surface ligand of $NaYF_4$:Nd/$NaDyF_4$ NCs, which not only provides good biocompatibility but also enhances tumor penetration of imaging nanoprobes. Most importantly, the current research demonstrates that $NaYF_4$:Nd/$NaDyF_4$ NCs are potential candidates as a multimodal bioimaging platform to obtain more accurate imaging information and sensitivity.

Results and discussion

The preparation process of Lipo-$NaYF_4$:Nd/$NaDyF_4$ NCs is schematically illustrated in Fig. 1a. First, uniform oleic acid (OA)-capped $NaYF_4$:Nd NCs were prepared using a solvothermal
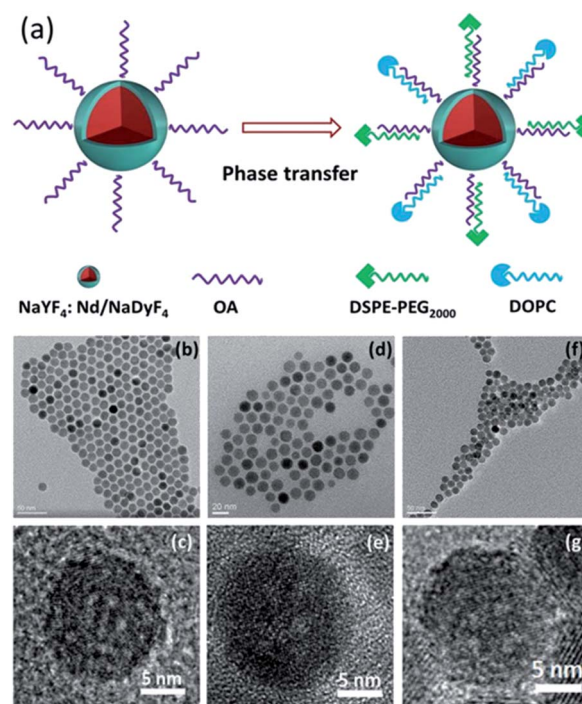

Fig. 1 (a) Schematic illustration of Lipo-$NaYF_4$:Nd/$NaDyF_4$ NCs. Typical and high resolution TEM images of OA-$NaYF_4$:Nd (b and c), OA-$NaYF_4$:Nd/$NaDyF_4$ (d and e) and Lipo-$NaYF_4$:Nd/$NaDyF_4$ (f and g) NCs, respectively.

method and could be well dispersed in cyclohexane. Subsequently, the $NaYF_4$:Nd NCs were used as seed particles and coated with a layer of $NaDyF_4$ as the shell to form OA-$NaYF_4$:Nd/$NaDyF_4$ core–shell NCs. In order to be applied in biological environments, the surface modification of the as-obtained $NaYF_4$:Nd/$NaDyF_4$ NCs is required to make them water-soluble and biocompatible. Finally, the OA-$NaYF_4$:Nd@$NaDyF_4$ NCs were modified with phospholipids as the capping ligand, which is considered to be safe and been widely used for encapsulating drugs. The transmission electron microscopy (TEM) images of the OA-$NaYF_4$:Nd, OA-$NaYF_4$:Nd/$NaDyF_4$, and Lipo-$NaYF_4$:Nd/$NaDyF_4$ NCs are shown in Fig. 1. The OA-$NaYF_4$:Nd NCs exhibit good uniformity with an average diameter of 12.6 nm (Fig. 1b), whereas the corresponding OA-$NaYF_4$:Nd/$NaDyF_4$ core–shell NCs have an average diameter of 15.7 nm (Fig. 1d). The thickness of the $NaDyF_4$ shells in the $NaYF_4$:Nd/$NaDyF_4$ core–shell NCs is about 1.5 nm. After surface modification, the amphiphilic PEGylated Lipo-$NaYF_4$:Nd/$NaDyF_4$ NCs displayed excellent water dispersal without any visible aggregation and were monodisperse in size, as shown in the TEM image (Fig. 1f). Furthermore, the high resolution TEM (HRTEM) image shown in Fig. 1c demonstrates that the synthesized OA-$NaYF_4$:Nd NCs possess clear lattice fringes, indicating high crystallinity of the obtained $NaYF_4$:Nd NCs. After coating with $NaDyF_4$ as the shell, the size of the obtained core–shell NCs increased slightly and the crystal lattice is clear, as shown in Fig. 1d and e. For subsequent biological application, the OA-$NaYF_4$:Nd/$NaDyF_4$ NCs were transferred from the organic phase to the aqueous phase using biomimetic phospholipids (Fig. 1a). After modification with the phospholipid, the size of the NCs was almost unchanged. The obtained Lipo-$NaYF_4$:Nd/$NaDyF_4$ core–shell NCs were still monodisperse in size (Fig. 1f and g). When the surface of the OA-NCs is modified with PEGylated phospholipids, the hydrophilic PEG on the surface of the NCs is exposed to water, which generates water dispersible NCs with a biomimetic and biocompatible surface.[15] The van der Waals interactions between the OA ligands on the NCs' surface and the two hydrophobic tails of the phospholipids make the Lipo-$NaYF_4$:Nd/$NaDyF_4$ core–shell NCs excellent water dispersal systems. In particular, the Lipo-$NaYF_4$:Nd/$NaDyF_4$ NCs can remain stable in aqueous dispersion for up to six months and in 50% FBS dispersion for at least one month.

The X-ray diffraction (XRD) patterns of the $NaYF_4$:Nd NCs (Fig. 2) show that all peaks match well with the pure hexagonal $NaYF_4$ phase (JCPDS no. 16-0334) and no impurity phase is observed. The strong and narrow peaks are evidence of the high crystallinity of the NCs, consistent with the results of TEM. It is worth noting that the lattice mismatch between hexagonal-phase $NaLnF_4$ was considered to be one of the key factors for the formation of core–shell NCs.[56,57] The patterns of the $NaYF_4$:Nd/$NaDyF_4$ NCs were slightly shifted relative to the standard hexagonal phase pattern of $NaDyF_4$ (JCPDS no. 27-0687), which is also attributed to the lattice mismatch between $NaYF_4$ and $NaDyF_4$. Energy dispersive X-ray spectroscopy (EDS) further confirms the presence of Y, Nd, Na, Dy and F elements in the $NaYF_4$:Nd/$NaDyF_4$ core–shell NCs (Fig. S1 in the ESI†). The Dy element exists in the EDS results of the $NaYF_4$:Nd/

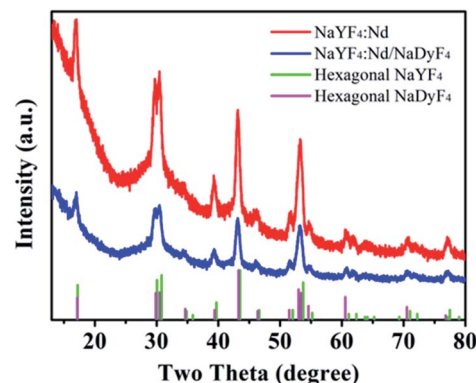**Fig. 2** XRD patterns of the as-synthesized $NaYF_4$:Nd (red) and $NaYF_4$:Nd/$NaDyF_4$ (blue) nanoparticles and corresponding standard curves (green, magenta).

$NaDyF_4$ core–shell NCs, indicating the successful coating of $NaDyF_4$ on the $NaYF_4$:Nd NCs.

The luminescence emission spectra of the obtained NCs were recorded and are shown in Fig. 3. Under excitation with a continuous-wave 785 nm laser, the emission spectra of the OA-$NaYF_4$:Nd NCs and the OA-$NaYF_4$:Nd/$NaDyF_4$ NCs in cyclohexane, and the Lipo-$NaYF_4$:Nd/$NaDyF_4$ NCs in saline display two characteristic downconversion emission peaks at 1058 and 1332 nm (Fig. 3), which are attributed to the transitions of Nd^{3+} from the $^4F_{3/2}$ state to the $^4I_{11/2}$ and $^4I_{13/2}$ states, respectively. After coating with the $NaDyF_4$ shell layer, the NIR-II fluorescence intensities of Nd^{3+} ions in the OA-$NaYF_4$:Nd/$NaDyF_4$ NCs at the emission peaks of 1058 nm and 1332 nm are increased to be 3.46- and 1.75-fold higher than that of the bare OA-capped $NaYF_4$:Nd NCs, respectively. In the process of crystal growth, lattice defects are inevitable. There are more defects on the surface of nanomaterials because of the large surface-volume ratio of the samples.[58] These defects are usually the centers of fluorescence quenching.[59] The outer passivation shell can effectively enhance the luminescence emission intensity of the NCs due to the partial elimination of surface defects in the NCs.[60] Similar observations have been reported.[39] Additionally,
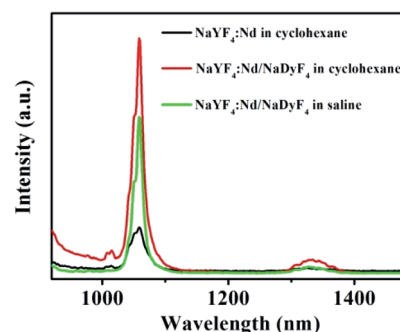

Fig. 3 Luminescence emission spectra of OA-$NaYF_4$:Nd NCs in cyclohexane (black), OA-$NaYF_4$:Nd/$NaDyF_4$ NCs in cyclohexane (red) and Lipo-$NaYF_4$:Nd/$NaDyF_4$ NCs in saline (green) solution under excitation of 785 nm.

the Lipo-NaYF$_4$:Nd/NaDyF$_4$ NCs could be dispersed in saline solution after surface modification with phospholipids and the intensity of luminescence emission remains strong enough, as shown in Fig. 3. The emission intensity of the Lipo-NaYF$_4$:Nd/NaDyF$_4$ NCs was slightly decreased in the saline phase in comparison with the OA-NaYF$_4$:Nd/NaDyF$_4$ NCs in cyclohexane. These well-defined emission bands are very suitable for deep tissue fluorescence biological imaging, matching well with the NIR-II biological windows.

Inspired by the excellent performance of Lipo-NaYF$_4$:Nd/NaDyF$_4$ NCs, the potential for multimodal imaging would be desired to explore their applications in the *in vitro* and *in vivo* bioimaging. The cytotoxicity of Lipo-NaYF$_4$:Nd/NaDyF$_4$ NCs as imaging contrast agents was evaluated against HeLa cells using the methyl thiazolyl tetrazolium (MTT) assay before biological applications. The cell viability of HeLa cells is demonstrated in Fig. 4 after incubation with Lipo-NaYF$_4$:Nd/NaDyF$_4$ NCs with a series of concentrations (0, 50, 100, 150, 200, 250, 300 and 400 μg mL^{-1}) for 12 h at 37 °C. The cell viability still remains above 90% even after incubation with an extremely high concentration (400 μg mL^{-1}) for 12 h. This result proves that the Lipo-NaYF$_4$:Nd/NaDyF$_4$ NCs have excellent biocompatibility within the appropriate concentration range, which is a very significant parameter for further research on biological applications.

To verify the NIR-II imaging in cells, the Lipo-NaYF$_4$:Nd/NaDyF$_4$ NCs with different concentrations (0, 1.5, 3.0, 6.0, 12.0, and 24.0 μg mL^{-1}) were transfected into HeLa cells *via* electroporation. The strong NIR emission of HeLa cell pellets after labeling with Lipo-NaYF$_4$:Nd/NaDyF$_4$ NCs was observed using an InGaAs camera under 808 nm irradiation. As shown in Fig. S2 in the ESI,† the NIR-II emission intensity of the fluorescence images increases with the increased NC concentration, which is attributed to dose-dependent cellular internalization.[15] This result shows that Lipo-NaYF$_4$:Nd/NaDyF$_4$ NCs can successfully penetrate the cell membrane and label effectively the HeLa cells.

To further confirm the internalization of Lipo-NaYF$_4$:Nd/NaDyF$_4$ NCs, the images of T_2-weighted MRI were collected after

the HeLa cells were labeled with different concentrations of Lipo-NaYF$_4$:Nd/NaDyF$_4$ NCs *via* electroporation. *In vitro* MRI was then performed on cell pellets packed in capillaries, which was considered a better mimic of *in vivo* tissues than cells diluted in culture media. MRI reveals more three-dimensional details of relative positions than other imaging methods including optical imaging.[61] Due to the short electronic relaxation time and the high magnetic moment, the Dy-doped NCs are considered an appropriate contrast agent for T_2-weighted MRI, especially for soft tissues.[62] In order to evaluate the MRI capacity of the Lipo-NaYF$_4$:Nd/NaDyF$_4$ NCs, the transverse relativity (r_2) was measured first. As shown in Fig. 5a, the T_2-weighted MRI displays a strong dependence of signal intensity on the Dy^{3+} concentration. The r_2 value of 44.0 mM^{-1} s^{-1} for Lipo-NaYF$_4$:Nd/NaDyF$_4$ NCs was calculated from the slope of the concentration-dependent relaxation rate ($1/T_2$), which was much higher than that of the previous report (7.68 mM^{-1} s^{-1} for Dy NCs).[47] In the previous report, the r_2 value of superparamagnetic iron oxide NPs is about 44.79 mM^{-1} s^{-1}, whereas commercial Resovist has an r_2 value of 151 mM^{-1} s^{-1}.[63] The r_2 value is dependent on the size of the nanocrystal clusters.[64] In our case, we speculate that compared with the commercial contrast agent, the relatively lower r_2 value may be attributed to the smaller size of the Lipo-NaYF$_4$:Nd/NaDyF$_4$ NCs. These results demonstrate the strong negative contrast effect and great potential utility of Lipo-NaYF$_4$:Nd/NaDyF$_4$ NCs for MRI. Therefore, a set of T_2-weighted MRI experiments were carried out to investigate the ability of accumulation of Lipo-NaYF$_4$:Nd/NaDyF$_4$ NCs in the HeLa cells after electroporation. Fig. 5b shows *in vitro* T_2-weighted MRI of HeLa cells labeled with Lipo-NaYF$_4$:Nd/NaDyF$_4$ NCs as a function of the added NC concentration. The Lipo-NaYF$_4$:Nd/NaDyF$_4$ solutions became darker in the T_2-weighted MRI with increasing the Dy^{3+} concentration. The T_2-weighted MRI demonstrated an obvious signal increase. This result shows that the Lipo-NaYF$_4$:Nd/NaDyF$_4$ NCs can be
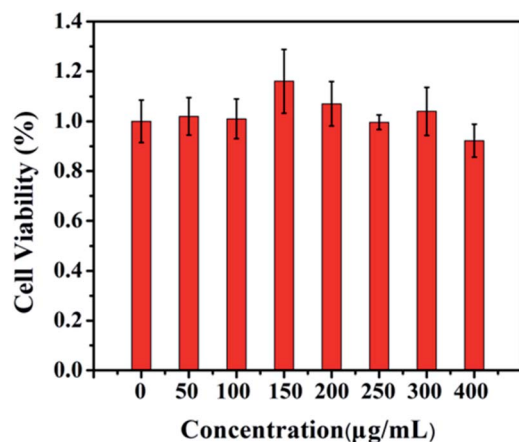

Fig. 4 Cell viability of HeLa cells after incubation with Lipo–NaYF$_4$:Nd/NaDyF$_4$ NCs with different concentrations for 12 h at 37 °C.
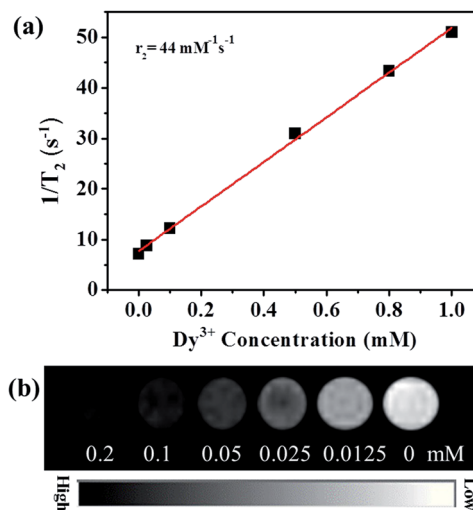

Fig. 5 (a) T_2 relaxivity plot of Lipo–NaYF$_4$:Nd/NaDyF$_4$ NCs dispersed in saline. (b) T_2-weighted MRI of HeLa cells after being transfected with Lipo–NaYF$_4$:Nd/NaDyF$_4$ NCs using an 11.7 T MR system.

considered to be an excellent candidate acting as a T_2-weighted contrast agent. The obtained Lipo-NaYF$_4$:Nd/NaDyF$_4$ NCs demonstrate not only high r_2 transverse relaxation but also excellent NIR-II fluorescence emission, which prevent effectively a common fluorescence quenching that often occurs in the nanocomposite containing iron oxide as T_2-weighted contrast agents. Therefore, multifunctional Lipo-NaYF$_4$:Nd/NaDyF$_4$ NCs as a multimodal platform would have potential application in NIR-II fluorescence and MR imaging.

Owing to the excellent performances of the Lipo-NaYF$_4$:Nd/NaDyF$_4$ NCs *in vitro*, the *in vivo* dual-mode bioimaging was carried out after the Lipo-NaYF$_4$:Nd and Lipo-NaYF$_4$:Nd/NaDyF$_4$ NCs (2.0 mg mL^{-1}) dissolved in saline were injected respectively into the tumors grown on the back of the nude mouse. In order to further evaluate the potential application of Lipo-NaYF$_4$:Nd/NaDyF$_4$ NCs for *in vivo* imaging, the NIR-II fluorescence imaging of the whole mouse was performed under 808 nm diode laser irradiation (0.12 W cm^{-2}) and the NIR-II fluorescence generated by Nd^{3+} was recorded using an InGaAs camera in the 900–1700 nm spectral range. The photograph and NIR-II fluorescence image of the whole body of the mouse are shown in Fig. 6a and b, respectively. The strong NIR-II fluorescence signals from the Lipo-NaYF$_4$:Nd/NaDyF$_4$ NCs can be clearly observed in the right tumor (yellow circle) on the back region of the cervical tumor bearing mouse in comparison with the left tumor (yellow circle), as displayed in Fig. 6b. Furthermore, the corresponding *in vivo* T_2-weighted MRI was performed to evaluate the capability of the Lipo-NaYF$_4$:Nd/NaDyF$_4$ NCs as contrast agents. An obviously darker signal was observed in T_2-weighted MRI of the right tumor in contrast with the left tumor, as shown in Fig. 6c, where the boundary between the normal soft tissue and the tumor is clearly visible. Thus, the tumor is easily distinguished. More importantly, both the NIR-II fluorescence signal and T_2-weighted MRI contrast were enhanced simultaneously in the right tumor injected with the Lipo-NaYF$_4$:Nd/NaDyF$_4$ NCs, which can provide more comprehensive imaging information and lead to higher diagnostic accuracy due to the resolution of MRI location at the sub-millimeter level.
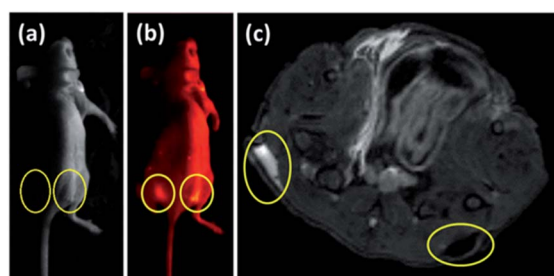
Fig. 6 (a) Photograph of a nude mouse implanted with HeLa cells. The positions of the two tumor regions are marked by yellow circles. The *in vivo* NIR-II fluorescence (b) and T_2-weighted MR imaging (c) of tumor regions after being directly injected with Lipo-NaYF$_4$:Nd (left) and Lipo-NaYF$_4$:Nd/NaDyF$_4$ (right) NCs, respectively. The fluorescence and negative contrast originating from Lipo-NaYF$_4$:Nd/NaDyF$_4$ NCs is clearly observed at the injection site (right circle), while the tumor (left circle) acts as a reference with the injected Lipo-NaYF$_4$:Nd NCs.

Accordingly, self-confirmed multimodal imaging based on MR and NIR-II fluorescence imaging of Lipo-NaYF$_4$:Nd/NaDyF$_4$ NCs would be desired for further accurate next generation diagnosis of tumors.

Experimental section

Chemicals

Yttrium chloride hexahydrate (YCl$_3$·6H$_2$O, 99.99%), neodymium chloride hexahydrate (NdCl$_3$·6H$_2$O, 99.99%) and dysprosium oxide (Dy$_2$O$_3$, 99.99%) were purchased from Jinan Camolai Trading Co., China. OA (90%), 1-octadecene (ODE, 90%) and trifluoroacetic acid (TFA, 99%) were purchased from Aldrich. 1,2-Distearoyl-*sn*-glycero-3-phosphoethanolamine-*N*-[methoxy (polyethyleneglycol)-2000] (ammonium salt) (DSPE-PEG$_{2000}$) and 1,2-dioleoyl-*sn*-glycero-3-phosphocholine (DOPC) were purchased from Avanti Polar Lipids, Inc. All the chemicals related with this work were of analytical grade and were used without any further purification.

Synthesis of Nd^{3+}-doped NaYF$_4$ NCs

Hexagonal-phase NaYF$_4$: 5% Nd NCs were synthesized following a solvothermal method in our previous work with slight modification.[11,12,14,65] In a typical experiment, 18 mg NdCl$_3$·6H$_2$O and 288 mg YCl$_3$·6H$_2$O were added into a 100 mL three-necked flask containing 6 mL OA and 15 mL ODE and then the solution was maintained at 160 °C for 1 h under an argon atmosphere. After being cooled down to room temperature, 10 mL methanol solution of NaOH (100 mg) and NH$_4$F (148 mg) were added and the mixture was stirred at room temperature for 1 h, followed by evaporating water and methanol at 120 °C. After degassing, the solution was heated to 300 °C and kept for 1 h, then cooled down to room temperature and the products were obtained by washing with ethanol several times, and finally re-dispersed in cyclohexane for future use.

Preparation of dysprosium trifluoroacetic acid precursors

The dysprosium trifluoroacetic acid (TFA) precursors were prepared from the corresponding oxides and TFA. Specifically, 0.013 mmol Dy$_2$O$_3$ was mixed with TFA (8 mL) and distilled water (10 mL) in a 50 mL three-neck round-bottom flask. The mixture was kept under magnetic stirring at 80 °C overnight until a transparent solution was formed. After that, the excess TFA and water were slowly evaporated by lowering the temperature to 60 °C. The final solid products were collected and put into a brown bottle and then stored in a desiccator.

Synthesis of OA-capped NaYF$_4$:Nd/NaDyF$_4$ core–shell NCs

A mixture of 0.5 mmol of Dy(CF$_3$COO)$_3$ and 0.5 mmol of NaCF$_3$COO was put into a 50 mL flask containing OA (6 mL) and ODE (15 mL). After stirring at room temperature for 10 min, 4 mL of cyclohexane containing 0.05 mmol of NaYF$_4$:Nd NCs was added to the mixture. Then, the solution mixture was slowly heated to 100 °C and kept for 30 min until the solution became clear. Then, under the protection of an argon atmosphere, water and air in the reaction system were removed. After that, the

reaction system was heated to 280 °C and maintained for 1 h. The final OA-NaYF$_4$:Nd/NaDyF$_4$ core–shell NCs were collected by centrifugation at 11 000 rpm and washed with ethanol three times.

Surface modification of NaYF$_4$:Nd/NaDyF$_4$ NCs with phospholipids

Lipo-NaYF$_4$:Nd/NaDyF$_4$ NCs were synthesized according to a published method with minor modifications.[15,66,67] DSPE-PEG$_{2000}$ (40 mg) and DOPC (5 mg) phospholipids were added into 2 mL chloroform. The OA-capped NaYF$_4$:Nd/NaDyF$_4$ NCs in chloroform (0.5 mL, 10 mg mL^{-1}) was mixed with the above chloroform solution (2 mL) in a round-bottom flask (10 mL). The mixed solution was sonicated for 30 min. To evaporate the solvent, the mixed solution was maintained at 60 °C for 60 min under vacuum in a rotary evaporator and a lipid film formed on the inside wall of the flask. Subsequently, the lipid film was hydrated with 1.5 mL of physiological saline. After vigorous sonication, the obtained NaYF$_4$:Nd/NaDyF$_4$ NCs became soluble. The solution was transferred to a microtube and centrifuged gently. The pellet was discarded to remove possible large aggregates. Excess lipids were removed from the Lipo-NaYF$_4$:Nd/NaDyF$_4$ NCs by ultracentrifugation and washing. The obtained Lipo-NaYF$_4$:Nd/NaDyF$_4$ NCs were finally suspended in saline water and stored at 4 °C in a fridge for further experiments. The preparation of Lipo-NaYF$_4$:Nd NCs was carried out by a similar procedure.

Cell culture and MTT assay

HeLa cells were cultured in Dulbecco's Modified Eagle Medium (DMEM) supplemented with 10% fetal bovine serum (FBS) and 1% penicillin/streptomycin at 37 °C in a humidified 5% CO$_2$ atmosphere. The cytotoxicity of Lipo-NaYF$_4$:Nd/NaDyF$_4$ NCs was measured using MTT assay. Cells were seeded into a 96-well culture plate with a density of 10^4 per well and incubated for 24 h under the same culture conditions as used previously. After that, the medium was washed with phosphate-buffered saline (PBS) and replaced with DMEM solution of Lipo-NaYF$_4$:Nd/NaDyF$_4$ NCs with different concentrations (0, 50, 100, 150, 200, 250, 300, and 400 μg mL^{-1}). The cells were then incubated for 12 h followed by calculating the cell viability with a typical MTT assay.

In vitro NIR-II photoluminescence imaging of Lipo-NaYF$_4$:Nd/NaDyF$_4$ NCs

In our experiment, the electroporation method was used to transfect the Lipo-NaYF$_4$:Nd/NaDyF$_4$ NCs into the cells instead of cultivation for several hours. Specifically, HeLa cells were detached using trypsin and harvested by 1000 rpm centrifugation for 4 min. HeLa cells were resuspended with transfer buffer with different Nd^{3+} concentrations of Lipo-NaYF$_4$:Nd/NaDyF$_4$ NCs (0, 1.5, 3.0, 6.0, 12.0, and 24.0 μg mL^{-1}). Subsequently, the HeLa cells were loaded into 96-well culture plates. Then, the mixture was treated with electrical pulses provided by the electroporation device (Etta Biotech X-Porator H1), centrifuged and washed with DMEM (only supplemented with 1%

penicillin/streptomycin) several times to remove the free Lipo-NaYF$_4$:Nd/NaDyF$_4$ NCs. The NIR-II fluorescence imaging of HeLa cells was performed by excitation using an 808 nm diode laser.

Relaxivity and T_2-weighted MRI of Lipo-NaYF$_4$:Nd/NaDyF$_4$ NCs in vitro

Different concentrations of Lipo-NaYF$_4$:Nd/NaDyF$_4$ NCs (10 μL, 0, 0.025, 0.1, 0.5, 0.8, and 1.0 mM) were distributed in capillary tubes. The transversal relaxation times (T_2) were measured using an 11.7 T Bruker-Biospin MRI scanner (60 MHz, 21 °C). The relaxation rates ($1/T_2$) were then plotted corresponding to the Dy^{3+} concentrations, and the relaxivities (r_2) were calculated from the slope of the graphs. A series of Lipo-NaYF$_4$:Nd/NaDyF$_4$ NCs in saline solutions (0, 0.0125, 0.025, 0.05, 0.1, and 0.2 mM of the Dy^{3+} concentration) for relaxivities have also been employed for in vitro cell MRI.

MRI and NIR-II fluorescence imaging in vivo

Nude mice (4 week aged, 20 g) were purchased from SLRC Laboratory Animal Co., Ltd. (Shanghai, China) and kept in the facility with free access to food and water. All animals received humane care in compliance with the Guide for the Care and Use of Laboratory Animals by the National Institute of Health. The study protocol was approved by the Laboratory Animal Ethics Committee. To perform in vivo imaging studies, the nude mice were injected with 5 million HeLa cells for induction of tumors. After 14 days of tumor growth, the Lipo-NaYF$_4$:Nd and Lipo-NaYF$_4$:Nd/NaDyF$_4$ NCs in physiological saline (20 μL, 2 mg mL^{-1}) were injected directly into the tumors and imaged using a T_2-weighted relaxation enhancement sequence with TR = 3000 ms, TE = 38 ms, slice thickness = 0.5 mm, and field of view (FOV) = 40 mm and an NIR fluorescence imaging system equipped with an InGaAs/SWIR camera (Photonic Science, UK and an 808 nm long pass filter) and an 808 nm diode laser.

Characterization

The TEM images and EDS spectra were obtained by using an FEI Tecnai G2 F20 S-Twin microscope operating at 200 kV. The power XRD patterns were recorded on a Bruker D8 Advance X-ray diffractometer (Cu Kα, operated at 40 kV, λ = 0.15406 nm) over the 2θ range of 10–80° with a scanning rate of 4° per minute. The NIR fluorescence spectra were recorded using a Model NS1 NanoSpectralyzer at room temperature using an excitation laser source of 785 nm. The collected range was from 900 to 1700 nm. MRI of phantoms was performed on a Bruker AVANCE 500WB spectrometer (Bruker NMR, Germany), with an 89 mm vertical-bore magnet of 11.7 T using a 15-mm-i.d. bird-cage coil. T_2 relaxation times of different Dy concentrations were measured using a multi-slice multi-echo (MSME) sequence with 20 echoes. The experimental parameters were TR = 3000 ms, TE = 40 ms, FOV = 12 mm × 12 mm, matrix = 96 × 96, slice thickness = 0.8 mm, and an average number = 2. T_2 relaxation rates were characterized by using the reciprocal of T_2 relaxation times. Transverse relaxivity (r_2) in the unit of (mM)$^{-1}$

s^{-1} was calculated using curve-fitting of the T_2 relaxation rates *versus* the Dy concentration (mM). The MSME method was used and TR/TE values were set as 500 ms/5.2 ms and 7500 ms/40 ms for T_2-weighted MRI. For all *in vitro* experiments, the experimental parameters were FOV = 12×12 mm, matrix = 96×96, and slice thickness = 0.8 mm. Inductively coupled plasma atomic emission spectroscopy (ICP-AES) (Agilent 5100) was employed to analyze the element concentrations in the Lipo-$NaYF_4$:Nd/$NaDyF_4$ NCs.

Conclusions

In summary, Lipo-$NaYF_4$:Nd/$NaDyF_4$ NCs have been developed as imaging contrast agents for multimodal self-confirmed NIR-II fluorescence and MR imaging of cancer cells *in vitro* and tumors *in vivo*. Owing to the partial elimination of surface defects of the $NaYF_4$:Nd NCs coated with the $NaDyF_4$ layer, the NIR-II fluorescence intensities of Nd^{3+} ions in core–shell NCs at 1058 nm and 1332 nm are 3.46- and 1.75-fold higher than that of the bare $NaYF_4$:Nd^{3+} NCs, respectively. The formed multifunctional Lipo-$NaYF_4$:Nd/$NaDyF_4$ NCs are water-dispersible and stable, and exhibit a low cytotoxicity at concentrations up to 400 μg mL^{-1}. Additionally, a high r_2 relaxivity of 44.0 mM^{-1} s^{-1} was calculated. More importantly, the Lipo-$NaYF_4$:Nd/ $NaDyF_4$ NCs provide a new strategy as imaging contrast agents for simultaneously enhanced NIR-II fluorescence and T_2-weighted MR imaging, which can provide more comprehensive imaging information to improve diagnostic accuracy of tumors and make them more competitive in next generation bioimaging fields.

Author contributions

Both Junwei Zhao and Xin Wang contributed to analysis of the data and writing the manuscript. Huishan Hu carried out the synthesis of materials and the characterization experiments of the as-synthesized samples. Wenquan Liu contributed to analysis of the data. Xin Wang contributed to the conception and design of the experiment. All authors reviewed the manuscript.

Conflicts of interest

There are no conflicts to declare.

Acknowledgements

Notes and references

1 P. Mi, D. Kokuryo, H. Cabral, H. Wu, Y. Terada, T. Saga, I. Aoki, N. Nishiyama and K. Kataoka, *Nat. Nanotechnol.*, 2016, **11**, 724–730.

2 M. A. Sowers, J. R. McCombs, Y. Wang, J. T. Paletta, S. W. Morton, E. C. Dreaden, M. D. Boska, M. F. Ottaviani, P. T. Hammond, A. Rajca and J. A. Johnson, *Nat. Commun.*, 2014, **5**, 5460.

3 G. Hong, Y. Zou, A. L. Antaris, S. Diao, D. Wu, K. Cheng, X. Zhang, C. Chen, B. Liu, Y. He, J. Z. Wu, J. Yuan, B. Zhang, Z. Tao, C. Fukunaga and H. Dai, *Nat. Commun.*, 2014, **5**, 4206.

4 A.-C. F. Jean-Luc Bridot, S. Laurent, C. Rivière, C. Billotey, B. Hiba, M. Janier, V. Josserand, J.-L. Coll, L. Vander Elst, R. Muller, S. Roux, P. Perriat and O. Tillement, *J. Am. Chem. Soc.*, 2007, **129**, 5076–5084.

5 G. Song, X. Zheng, Y. Wang, X. Xia, S. Chu and J. Rao, *ACS Nano*, 2019, **13**, 7750–7758.

6 T. E. Yankeelov, R. G. Abramson and C. C. Quarles, *Nat. Rev. Clin. Oncol.*, 2014, **11**, 670–680.

7 L. Wu, A. Mendoza-Garcia, Q. Li and S. Sun, *Chem. Rev.*, 2016, **116**, 10473–10512.

8 J. E. Lemaster, F. Chen, T. Kim, A. Hariri and J. V. Jokerst, *ACS Appl. Nano Mater.*, 2018, **1**, 1321–1331.

9 L. Jing, K. Ding, S. V. Kershaw, I. M. Kempson, A. L. Rogach and M. Gao, *Adv. Mater.*, 2014, **26**, 6367–6386.

10 S. Yan, X. Zeng, Y. Tang, B. F. Liu, Y. Wang and X. Liu, *Adv. Mater.*, 2019, **31**, 1905825.

11 X. Wu, Q. Zhang, X. Wang, H. Yang and Y. Zhu, *Eur. J. Inorg. Chem.*, 2011, **2011**, 2158–2163.

12 J. Zhao, H. Yang, J. Li, Y. Wang and X. Wang, *Sci. Rep.*, 2017, **7**, 18014.

13 J. Zhao, X. Li, X. Wang and X. Wang, *Nanoscale Res. Lett.*, 2019, **14**, 200.

14 J. Zhao, Z. Zhang and X. Wang, *J. Alloys Compd.*, 2020, **820**, 153142.

15 X. Wang, H. Hu, H. Zhang, C. Li, B. An and J. Dai, *Nano Res.*, 2018, **11**, 1069–1081.

16 X. Wang, Q. Zhang, J. Zhao and J. Dai, *J. Mater. Chem. B*, 2013, **1**, 4637–4643.

17 Q. Chen, X. Wang, F. Chen, Q. Zhang, B. Dong, H. Yang, G. Liu and Y. Zhu, *J. Mater. Chem.*, 2011, **21**, 7661–7667.

18 G. Hong, A. L. Antaris and H. Dai, *Nat. Biomed. Eng.*, 2017, **1**, 0010.

19 Y. Fan and F. Zhang, *Adv. Opt. Mater.*, 2019, **7**, 1801417.

20 Y. Zhong, Z. Ma, F. Wang, X. Wang, Y. Yang, Y. Liu, X. Zhao, J. Li, H. Du, M. Zhang, Q. Cui, S. Zhu, Q. Sun, H. Wan, Y. Tian, Q. Liu, W. Wang, K. C. Garcia and H. Dai, *Nat. Biotechnol.*, 2019, **37**, 1322–1331.

21 H. Li, X. Wang, X. Li, S. Zeng and G. Chen, *Chem. Mater.*, 2020, **32**, 3365–3375.

22 Y. Li, G. Bai, S. Zeng and J. Hao, *ACS Appl. Mater. Interfaces*, 2019, **11**, 4737–4744.

23 A. Benayas, F. Ren, E. Carrasco, V. Marzal Beneyto, B. del Rosal, B. Gonfa, A. Juarranz, F. Sanz-Rodriguez, D. Jaque,

J. Garcc-a-Soic, D. Ma and F. Vetrone, *Adv. Funct. Mater.*, 2015, **25**, 6650–6659.

24 H. Pan, P. Zhang, D. Gao, Y. Zhang, P. Li, L. Liu, C. Wang, H. Wang, Y. Ma and L. Cai, *ACS Nano*, 2014, **8**, 5468–5477.

25 G. Hong, J. T. Robinson, Y. Zhang, S. Diao, A. L. Antaris, Q. Wang and H. Dai, *Angew. Chem., Int. Ed.*, 2012, **51**, 9818–9821.

26 Y. Zhang, G. Hong, Y. Zhang, G. Chen, F. Li, H. Dai and Q. Wang, *ACS Nano*, 2012, **6**, 3695–3702.

27 R. Hu, W. C. Law, G. Lin, L. Ye, J. Liu, J. Liu, J. L. Reynolds and K. T. Yong, *Theranostics*, 2012, **2**, 723–733.

28 G. Hong, S. Diao, J. Chang, A. L. Antaris, C. Chen, B. Zhang, S. Zhao, D. N. Atochin, P. L. Huang, K. I. Andreasson, C. J. Kuo and H. Dai, *Nat. Photonics*, 2014, **8**, 723–730.

29 S. Diao, G. Hong, A. L. Antaris, J. L. Blackburn, K. Cheng, Z. Cheng and H. Dai, *Nano Res.*, 2015, **8**, 3027–3034.

30 G. Hong, S. Diao, A. L. Antaris and H. Dai, *Chem. Rev.*, 2015, **115**, 10816–10906.

31 A. L. Antaris, H. Chen, K. Cheng, Y. Sun, G. Hong, C. Qu, S. Diao, Z. Deng, X. Hu, B. Zhang, X. Zhang, O. K. Yaghi, Z. R. Alamparambil, X. Hong, Z. Cheng and H. Dai, *Nat. Mater.*, 2016, **15**, 235–242.

32 B. Li, L. Lu, M. Zhao, Z. Lei and F. Zhang, *Angew. Chem., Int. Ed.*, 2018, **57**, 7483–7487.

33 U. Rocha, K. U. Kumar, C. Jacinto, I. Villa, F. Sanz-Rodrc-guez, M.-a. del Carmen Iglesias de la Cruz, A. Juarranz, E. Carrasco, F. C. J. M. van Veggel, E. Bovero, J. G.-a. Soic and D. Jaque, *Small*, 2014, **10**, 1141–1154.

34 B. del Rosal, A. Perez, M. g. Misiak, A. Bednarkiewicz, A. Vanetsev, Y. Orlovskii, D. Jovanovic, M. Dramicanin, U. Rocha, K. Kumar, C. Jacinto, E. Navarro, E. Martc-n Rodrc-guez, M. Pedroni, A. Speghini, G. Hirata, I. Martin and D. Jaque, *J. Appl. Phys.*, 2015, **118**, 143104.

35 G. Chen, T. Y. Ohulchanskyy, S. Liu, W.-C. Law, F. Wu, M. T. Swihart, H. C gren and P. N. Prasad, *ACS Nano*, 2012, **6**, 2969–2977.

36 A. Bednarkiewicz, D. Wawrzynczyk, M. Nyk and W. Strek, *Opt. Mater.*, 2011, **33**, 1481–1486.

37 D. H. Ortgies, M. Tan, E. C. Ximendes, B. del Rosal, J. Hu, L. Xu, X. Wang, E. MartC-n Rodrc-guez, C. Jacinto, N. Fernandez, G. Chen and D. Jaque, *ACS Nano*, 2018, **12**, 4362–4368.

38 R. W. Mengyao Zhao, B. Li, Y. Fan, Y. Wu, X. Zhu and F. Zhang, *Angew. Chem., Int. Ed.*, 2018, **58**, 2050–2054.

39 F. Ren, L. Ding, H. Liu, Q. Huang, H. Zhang, L. Zhang, J. Zeng, Q. Sun, Z. Li and M. Gao, *Biomaterials*, 2018, **354**, 30–43.

40 I. Villa, A. Vedda, I. X. Cantarelli, M. Pedroni, F. Piccinelli, M. Bettinelli, A. Speghini, M. Quintanilla, F. Vetrone, U. Rocha, C. Jacinto, E. Carrasco, F. S. Rodrc-guez, C. n. Juarranz, B. del Rosal, D. H. Ortgies, P. H. Gonzalez, J. G.-a. Soic and D. J. Garcc-a, *Nano Res.*, 2015, **8**, 649–665.

41 X.-F. Yu, L.-D. Chen, M. Li, M.-Y. Xie, L. Zhou, Y. Li and Q.-Q. Wang, *Adv. Mater.*, 2008, **20**, 4118–4123.

42 Y. Chen, H. Chen, S. Zhang, F. Chen, S. Sun, Q. He, M. Ma, X. Wang, H. Wu, L. Zhang, L. Zhang and J. Shi, *Biomaterials*, 2012, **33**, 2388–2398.

43 H. Yang, Y. Zhuang, H. Hu, X. Du, C. Zhang, X. Shi, H. Wu and S. Yang, *Adv. Funct. Mater.*, 2010, **20**, 1733–1741.

44 L. Cheng, K. Yang, Y. Li, J. Chen, C. Wang, M. Shao, S.-T. Lee and Z. Liu, *Angew. Chem., Int. Ed.*, 2011, **50**, 7385–7390.

45 H. Yang, C. Zhang, X. Shi, H. Hu, X. Du, Y. Fang, Y. Ma, H. Wu and S. Yang, *Biomaterials*, 2010, **31**, 3667–3673.

46 Y. Luo, S. Du, W. Zhang, Z. Liao, F. Zuo and S. Yang, *RSC Adv.*, 2017, **7**, 37929–37937.

47 J. Zhou, Z. Lu, G. Shan, S. Wang and Y. Liao, *Biomaterials*, 2014, **35**, 368–377.

48 W. Yuan, D. Yang, Q. Su, X. Zhu, T. Cao, Y. Sun, Y. Dai, W. Feng and F. Li, *Adv. Funct. Mater.*, 2016, **26**, 8631–8642.

49 S. Viswanathan, Z. Kovacs, K. N. Green, S. J. Ratnakar and A. D. Sherry, *Chem. Rev.*, 2010, **110**, 2960–3018.

50 J. Zhou, Q. Liu, W. Feng, Y. Sun and F. Li, *Chem. Rev.*, 2015, **115**, 395–465.

51 W. Fan, W. Bu and J. Shi, *Adv. Mater.*, 2016, **28**, 3987–4011.

52 J. Jin, Z. Xu, Y. Zhang, Y.-J. Gu, M. H.-W. Lam and W.-T. Wong, *Adv. Healthcare Mater.*, 2013, **2**, 1501–1512.

53 G. Chen, I. Roy, C. Yang and P. N. Prasad, *Chem. Rev.*, 2016, **116**, 2826–2885.

54 J. Nam, N. Won, J. Bang, H. Jin, J. Park, S. Jung, S. Jung, Y. Park and S. Kim, *Adv. Drug Delivery Rev.*, 2013, **65**, 622–648.

55 S. Shanmugam, R. Baskaran, P. Balakrishnan, P. Thapa, C. S. Yong and B. K. Yoo, *Eur. J. Pharm. Biopharm.*, 2011, **79**, 250–257.

56 D. Liu, X. Xu, Y. Du, X. Qin, Y. Zhang, C. Ma, S. Wen, W. Ren, E. M. Goldys, J. A. Piper, S. Dou, X. Liu and D. Jin, *Nat. Commun.*, 2016, **7**, 10254.

57 B. Xu, X. Zhang, W. Huang, Y. Yang, Y. Ma, Z. Gu, T. Zhai and Y. Zhao, *J. Mater. Chem. B*, 2016, **4**, 2776–2784.

58 L. J. Tian, Y. J. Sun, Y. Yu, X. G. Kong and H. Zhang, *Chem. Phys. Lett.*, 2008, **452**, 188–192.

59 Y. Sun, Y. Chen, L. Tian, Y. Yu, X. Kong, J. Zhao and H. Zhang, *Nanotechnology*, 2007, **18**, 275609.

60 Y. Wang, L. Tu, J. Zhao, Y. Sun, X. Kong and H. Zhang, *J. Mater. Chem. C*, 2009, **113**, 7164–7169.

61 S. Carron, Q. Y. Li, L. Vander Elst, R. N. Muller, T. N. Parac-Vogt and J. A. Capobianco, *Dalton Trans.*, 2015, **44**, 11331–11339.

62 G. K. Das, N. J. J. Johnson, J. Cramen, B. Blasiak, P. Latta, B. Tomanek and F. C. J. M. van Veggel, *J. Phys. Chem. Lett.*, 2012, **3**, 524–529.

63 S. Josef, P. Katerina, H. Marketa, J. Ivan, M. Massimiliano, M. David, K. Lucia, S. Jan, P. Helena and G. Eva, *Int. J. Nanomed.*, 2014, **9**, 5355–5372.

64 E. Poselt, H. Kloust, U. Tromsdorf, M. Janschel, C. Hahn, C. Masslo and H. Weller, *ACS Nano*, 2012, **6**, 1619–1624.

65 Q. Zhang, X. Wang and Y. Zhu, *J. Mater. Chem.*, 2011, **21**, 12132.

66 L. L. Li, R. Zhang, L. Yin, K. Zheng, W. Qin, P. R. Selvin and Y. Lu, *Angew. Chem., Int. Ed.*, 2012, **51**, 6121–6125.

67 C. Yao, P. Wang, L. Zhou, R. Wang, X. Li, D. Zhao and F. Zhang, *Anal. Chem.*, 2014, **86**, 9749–9757.